Textile reinforced concrete members subjected to tension, bending, and in-plane loads: Experimental study and numerical analyses

Adam Sciegaj [a,b], Sebastian Almfeldt [c], Fredrik Larsson [d], Karin Lundgren [c,*]

[a] *Department of Mechanics of Materials and Structures, Faculty of Civil and Environmental Engineering, Gdańsk University of Technology, Gdańsk, Poland*
[b] *EkoTech Center, Gdańsk University of Technology, Gdańsk, Poland*
[c] *Department of Architecture and Civil Engineering, Chalmers University of Technology, Sweden*
[d] *Department of Industrial and Materials Science, Chalmers University of Technology, Sweden*

ABSTRACT

Textile reinforced concrete has raised increasing research interest during the last years, mainly due to its potential to be used for freeform shell structures involving complex load situations. Yet, most experimental work has focused on test setups with primarily uniaxial loading. In the current work, such setups are complemented with a novel test setup of deep beams, including in-plane bending and shear. Further, nonlinear finite element analyses were carried out, applying an earlier calibrated bond-slip relation and efficiency factors for strength and stiffness of the textile reinforcement. It was found that the structural behaviour in terms of the overall stiffness, ultimate load and deformation, number of cracks, and total (summed) crack width, could be described with reasonably good accuracy. The inclusion of a calibrated efficiency factor for the stiffness of the yarn was shown to be vital. Moreover, it was shown to be important to weaken and randomise the material properties of the concrete at the location of transverse yarns, to trigger localisation (cracking) in the numerical model.

1. Introduction

Textile Reinforced Concrete (TRC) is an interesting material with large potential. It has been used in practical applications for strengthening [1], in facades [2], as well as in a pedestrian bridge [3,4], and has been suggested for slabs [5–8]. One very interesting application is freeform shell structures [9–11]. With corrosion-resistant textiles, and thus small required covers, thin elements can be obtained. Freeform structures entail a multitude of complex load situations. Yet, in most experimental work, test setups with mainly uniaxial loading are commonly used. Some examples are pull-out tests [12–16], uniaxial tension tests [17–21], and one-way flexure tests [22–26]. There is limited experimental work addressing more complex load situations; some examples are biaxial tension tests [27], and loading of two-way slabs [28], and shells [29,30]. To enable the use of TRC in freeform structures, more experimental work including complex load situations is needed, such as in-plane bending and shear.

Further, there is a need to investigate how well analyses can be used to predict the behaviour in complex load situations. A recent review pointed out the need for generalised strategies for mechanical analysis of

TRC [31]. TRC is a complex material; each textile yarn consists of many filaments [32], and slip takes place both between the filaments and between the yarns and the adjacent concrete [33]. Accordingly, the whole tensile capacity of the yarns cannot be utilised when embedded in concrete. In analyses, it is therefore common to apply an efficiency factor for the strength, as first suggested by Hegger et al. [34] and subsequently used by several researchers, *e.g.*, [20,35–37]. However, interfilament slip will actually influence both strength and stiffness of the yarn. In recent work, the authors showed that analyses including a calibrated value of an efficiency factor for the stiffness improved the agreement between analyses and pull-out experiments [38]. Before this, only few researchers have applied an efficiency factor for the stiffness [39,40]. To further describe the structural behaviour of TRC in analyses, cracking of the concrete, as well as the slip and bond stress transfer between textile reinforcement yarns and concrete need to be included. The bond stress transfer is vital for the global structural behaviour of the composite [34,41], and is commonly included in modelling by applying a bond stress versus slip relation [26,42,43]. In earlier work of the authors [38], two-sided asymmetrical pull-out tests were carried out, and an indirect procedure to calibrate a bond-slip relation and efficiency

---

Table 1

Technical specifications of the carbon textile reinforcement, StoFRP Grid 1000C 390.

Parameter	Value	Comment
Young's modulus, E_0	242 GPa	From manufacturer
Tensile capacity, F_0	5500 N/yarn	From manufacturer
Fracture elongation	17 ‰	From manufacturer
Density, composite	390 g/m^2	From manufacturer
Density, carbon fibre	231 g/m^2	From manufacturer
Mesh free opening	34 mm	Measured, same in both directions
Yarn width	3.55 (0.46) mm	Measured, average and standard deviation
Yarn thickness	0.385 (0.075) mm	Measured, average and standard deviation

factors for strength and stiffness of the textile reinforcement in concrete was developed.

The aim of this work was to investigate how well analyses with a calibrated bond-slip relation and efficiency factors for strength and stiffness of the textile reinforcement can describe the behaviour in different load situations, including both mainly uniaxial stress states and more complex load situations, such as deep beams loaded in four-point bending. In such cases, the plane sections cannot be assumed to remain plane after deformation, and in addition, the effects of in-plane shear can be observed. To reach this aim, experiments were carried out, using both common test setups and one setup including a more complex load situation. The same materials as in earlier pull-out tests were used, to have knowledge on calibrated material parameters.

The remainder of the paper is structured as follows: Section 2 describes the experimental program, including materials, test setups and procedures. Section 3 describes the numerical models of the experiments and Section 4 describes the results of both experiments and finite element analyses. Finally, conclusions and an outlook to future work are presented in Section 5.

2. Experimental program

2.1. Overview

The experimental program consisted of three types of test setups: uniaxial tension tests, one-way flexure tests, and tests of deep beams. Two uniaxial tension tests and three of each of the other test types were conducted, with intentionally identical specimens for each test type. The specimens were named T for uniaxial tension, O for one-way flexure, and D for deep beams, while a,b,c were used to differ between the individual specimens of the same type. Pilot test series were conducted in student works during 2019–2020: one-way slabs in [44] and deep beams in [45], while the tests reported here were carried out in January 2021. The displacement field was monitored using Digital Image Correlation (DIC) in all tests; details are given in Section 2.4.

2.2. Materials and production

The concrete was produced from a commercial concrete mix, type StoCrete R 40 [46]. It contained cement of class CEM 1, and had a maximum grain size of 3 mm. The uniaxial compressive strength was measured in tests on cylinders according to standard [47], with an average value of 67.8 MPa.

The reinforcement was a carbon mesh, type StoFRP Grid 1000C 390. It had yarns of rectangular cross-section and material parameters as listed in Table 1. The textile grid was produced in factory environment in an automated process, aligning the fibre yarns in the desired directions and impregnating them with epoxy resin. The connections to yarns in the transverse direction were very weak.

At specimen production, the reinforcement mesh was kept in place by a wooden framework. All specimens were cast at the same time and tested after 28 to 30 days curing.

2.3. Test set-ups and procedure

2.3.1. Uniaxial tensile tests

The uniaxial tensile tests were carried out according to the

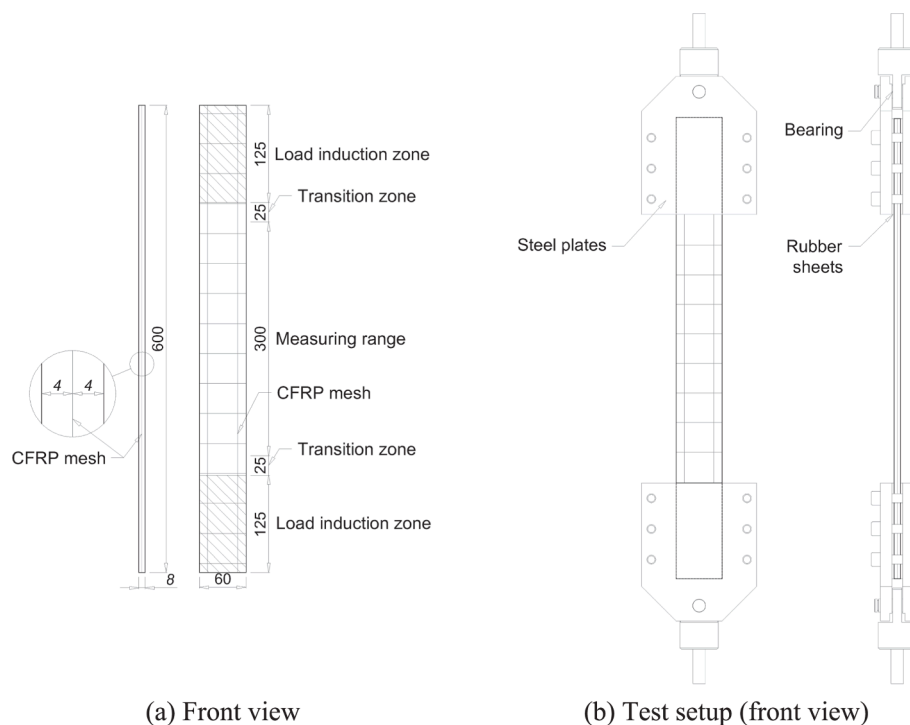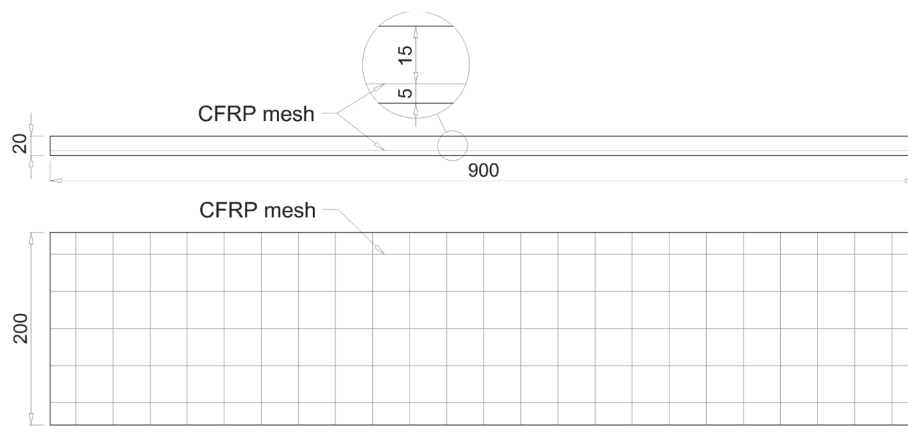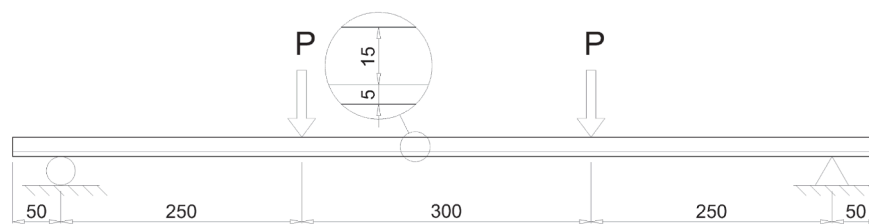
(a) Front view

(b) Test setup (front view)

Fig. 1. Uniaxial tension tests. (a) Drawing of specimens; measurements in mm; (b) Test setup.

(a) Top and side view

(b) Side view

Fig. 2. One-way bending tests of slabs. (a) Drawing of specimens; measurements in mm; (b) Test setup.

recommendations by RILEM TC 232-TDT [17]. The specimens were $60 \cdot 600 \cdot 8$ mm^3, see Fig. 1. A single layer of carbon mesh was placed centrally in the thickness direction. Clamps placed at the ends of the specimens (Fig. 1) were allowed to rotate, to avoid applying bending moment. Between the steel clamps and the concrete surface, 1.5 mm thick natural rubber sheets were used to get even pressure and increase friction. The bolts at the clamps were tightened by hand to a level sufficient to avoid slip in the clamps during testing yet avoiding crushing of the concrete at the clamps. At testing, load was applied by controlling the deformation between the clamps to a rate of 1.2 mm/min. At evaluation of the results from DIC measurements, the deformation over the mid 300 mm was used (marked as measuring range in Fig. 1) to avoid including possible slip at the clamps. Further, the crack width of each individual crack was evaluated from the DIC measurements as the displacement in the loading direction between two points situated on different sides of the individual crack.

2.3.2. One-way flexure tests

One-way flexure tests were carried out as four-point bending tests on thin slabs. The specimens were $200 \cdot 900 \cdot 20$ mm^3, see Fig. 2. A single layer of carbon mesh was placed with 5 mm cover. Four-point bending as shown in Fig. 2b was applied, with line loads and line supports across the width of the slabs. To enable good visibility of the crack pattern, the specimens were tested upside down. The two loads were applied by a hydraulic jack acting on a stiff load distribution beam in deformation control, with 3 mm/min of deformation at the hydraulic jack to a total deformation of 40 to 50 mm. At evaluation of the results, the mid-span deflection relative to the deflection at the loads was used. Further, the crack width of individual cracks was evaluated from the DIC measurements as the displacement in the direction along the slab span between
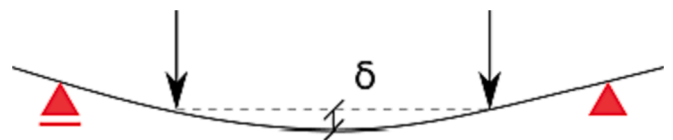
two points on each side of the individual crack.

To plot the force versus mid-span deflection, the latter was computed relative to the mean deflection at the point loads, see Fig. 3.

2.3.3. Tests of deep beams

As described in the introduction, there is a need for experiments including more complex loading situations than the commonly used test setups. Yet, a suitable test setup shall at the same time have well-defined loading, boundaries and be uncomplicated to carry out. These criteria led to the development of a test setup for deep beams, in which thin specimens were subjected to bending and shear in the plane of the specimen. The specimens were $200 \cdot 900 \cdot 20$ mm^3, see Fig. 4. Three layers of carbon mesh were placed with 5 mm cover, and 5 mm spacing between the layers.

Four-point bending as shown in Fig. 4b was applied; the two point loads were applied by a hydraulic jack acting on a stiff load distribution beam (Fig. 4d). Support and loading plates for vertical loads (Fig. 4e) were made of steel. At testing, a specimen was placed and centered in the 21 mm wide groove of the support plates, and the support plates were in turn placed on rollers. The grooves provided stability during
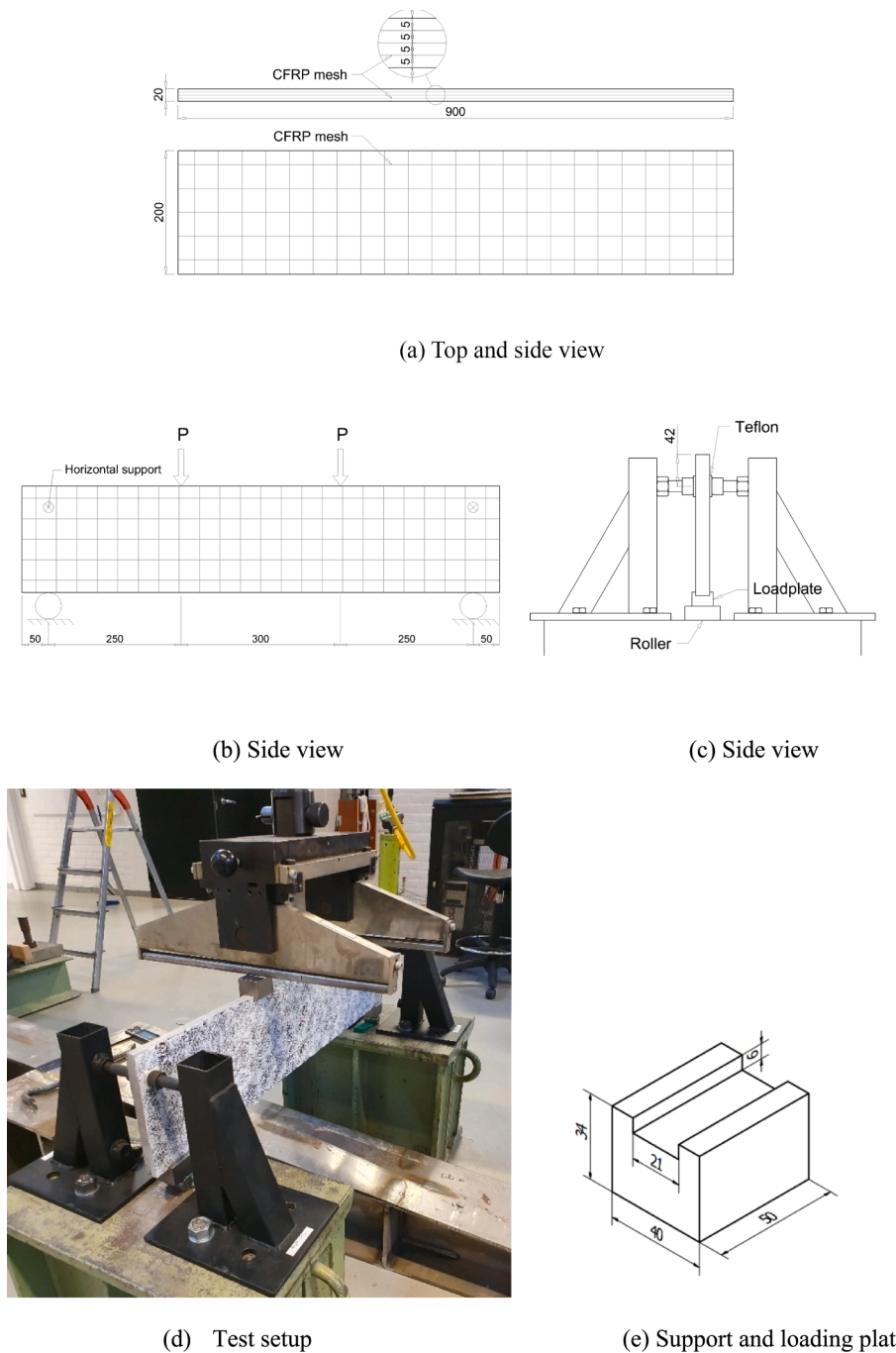

Fig. 3. Definition of beam mid-span deflection, δ, which was computed relative to deflection at point loads.

(a) Top and side view

(b) Side view

(c) Side view

(d)   Test setup

(e) Support and loading plate

Fig. 4. Tests of deep beams. (a) Drawing of specimens; measurements in mm; (b) Test set-up; (c) Drawing of test setup from the side, showing the arrangement of the vertical and horizontal supports; (d) Photo of the test setup (d) Drawing of vertical support and loading plates.

mounting of the test setup. Further, horizontal supports on both sides were applied at a height of 42 mm from top of the specimen, with Teflon sheets between the support and the specimen to allow transversal movement. These horizontal supports consisted of socket head bolts with an area acting on the Teflon sheets with an outer diameter of 21.5 mm. The bolts were carefully adjusted before testing to ensure a vertical placement of the test specimen. In addition, the bolts were tightened by hand to a level ensuring contact on both sides of the specimen yet allowing transversal movement. The DIC measurements were evaluated to ensure that transversal movement did indeed take place. At evaluation of the results, the mid-span deflection relative to the deflection at the loads was used. Further, the crack width of individual cracks was evaluated from the DIC measurements as the displacement between two

points along a line situated 25 mm above the bottom of the deep beam. The tests were carried out in deformation control, with the deformation rate of 0.25 mm/min at the hydraulic jack until all cracks were formed. Thereafter, the loading rate was increased to 1 mm/min. Similar to one-way flexure tests, the mid-span deflection was computed relative to the mean deflection at the point loads, see Fig. 3.

2.4. Digital image correlation during testing

During all tests, displacements and crack openings were captured with Digital Image Correlation (DIC), using GOM ARAMIS 12 M adjustable stereo camera system [48]. In the uniaxial tension tests (*T*-series), images were acquired with a frequency of 4 Hz, and 0.1 Hz in the

other tests (*D*- and *O*-series), respectively. The surfaces of the specimens were painted with a black and white high contrast speckled pattern allowing the software to produce full-field displacements and strains. The results were processed by the software GOM Correlate [49]. At evaluation of the test results, the crack widths were evaluated from the DIC measurements with virtual displacement transducers as described for each test type.

3. Numerical modelling

3.1. Overview

To investigate how well the calibrated bond-slip relation and efficiency factors for strength and stiffness describe the complex composite action of textile reinforced concrete, the experiments described in Section 2 were simulated numerically. All specimens were modelled using the software DIANA [50], and a corresponding nonlinear Finite Element (FE) analysis was considered for each test. Each experiment type (denoted either *T*, *O* or *D*) was simulated with two sets of input parameters (denoted *Input I* and *Input II*, cf. Fig. 6). The input sets differed regarding the constitutive model describing the bond-slip relation and the use of efficiency factors for the stiffness of the textile yarns, according to [38]. Furthermore, the concrete was weakened at the positions of the transverse yarns together with a random distribution of stiffness, strength and fracture energy (according to Eqs. (5)–(7) in the following section), upon which ten realisations were analysed for each of the two sets of input parameters. Thus, in total, sixty finite element simulations were carried out. In the following, the material models used in modelling are summarised, and the models used in individual analysis types are presented.

3.2. Material models

For the concrete, the Young's modulus, tensile strength and fracture energy were computed based on the measured compressive strength, according to Model Code 2010 [51]. A nonlinear material model with damage formulation both in tension and compression was used. In the linear range, the Young's modulus $E_c = 40.7$ GPa and a Poissson's ratio $\nu_c = 0.2$ were specified. The compressive behaviour was modelled using the stress versus strain behaviour suggested by Thorenfeldt [52], where the compressive strength of concrete was given as 67.8 MPa.

The stress–strain relation in compression can be expressed as

$$\sigma(\varepsilon) = -f_P \frac{\varepsilon}{\varepsilon_P} \left(\frac{n}{n - \left(1 - \left(\frac{\varepsilon}{\varepsilon_P}\right)^{nk}\right)} \right), \tag{1}$$

where f_P is the compressive peak stress and ε_P is the compressive peak strain. The parameters n and k are determined as

$$n = 0.80 + \frac{f_{cc}}{17}; \qquad k = \begin{cases} 1 & \text{if } \varepsilon_P \leq \varepsilon \leq 0 \\ 0.66 + \frac{f_{cc}}{62} & \text{if } \varepsilon \leq \varepsilon_{P}. \end{cases}, \tag{2}$$

where f_{cc} is the cube compressive strength of concrete.

In tension, a nonlinear tension softening model according to Hordijk et al. [53] was used. Within this setting, a tensile strength of 4.35 MPa and a fracture energy of 156 N/m were used. The crack band width was assumed to equal the mesh size. Hordijk tension softening describes the relation between the crack stress, σ_n, and the crack opening, w as:

$$\frac{\sigma_n(w)}{f_t} = \begin{cases} \left(1 + \left(c_1 \frac{w}{w_{ult}}\right)^3\right) e^{-c_2 \frac{w}{w_{ult}}} - \frac{w}{w_{ult}}\left(1 + c_1^3\right) e^{-c_2} & \text{if } w < w_{ult} \\ 0 & \text{if } w \geq w_{ult} \end{cases}, \tag{3}$$
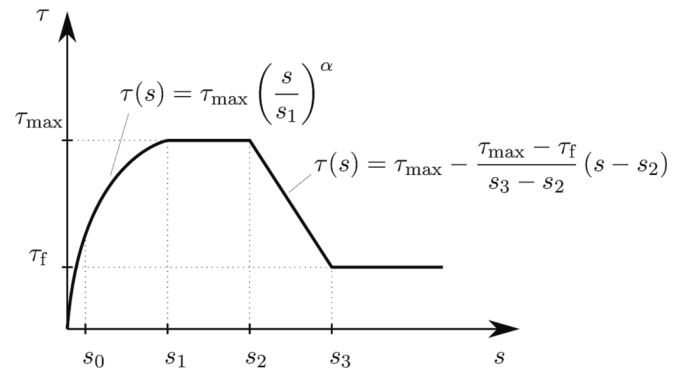

Fig. 5. Bond-slip model from Model Code 2010 [51], with seven parameters: s_0 - s_3, τ_{max}, τ_f, and α.

where $c_1 = 3$, and $c_2 = 6.93$. The ultimate crack opening, w_{ult} depends on the fracture energy, G_F, and the tensile strength, f_t as follows:

$$w_{ult} = 5.136 \frac{G_F}{f_t}. \tag{4}$$

To properly trigger localization (cracking), and to account for the variability of material parameters, the tensile strength, f_t, fracture energy, G_F, and the Young's modulus, E_c, of the concrete elements directly adjacent to transverse yarns were sampled from Gaussian distribution with the mean and variance taken as:

$$f_t \sim \mathcal{N}(\zeta \cdot 4.35 \text{ MPa}, \ 0.1 \ \text{MPa}^2), \tag{5}$$

$$G_F \sim \mathcal{N}(\zeta \cdot 156 \ \frac{\text{N}}{\text{m}}, \ 5 \ \frac{\text{N}^2}{\text{m}^2}), \tag{6}$$

$$E_c \sim \mathcal{N}(\zeta \cdot 40.7 \text{ GPa}, \ 0.5 \ \text{GPa}^2). \tag{7}$$

The reduction factor ζ reflects the conservation of volume in the model. Due to the presence of the transverse yarn, the volume of the concrete in the (weakened) element is effectively smaller. The reduction factor ζ thus depends on the mesh and reinforcement configuration and is given for each analysis type in the following sections, i.e., in Section 3.3.2 for the uniaxial tensile tests, in Section 3.3.3 for one-way flexure tests, and in Section 3.3.4 for tests on deep beams.

For the textile reinforcement, Young's modulus, E_0, was specified as 242 GPa according to Table 1. Uneven stress distribution within the yarn motivated the introduction of an efficiency factor for the stiffness, η_E:

$$E = \eta_E E_0 \tag{8}$$

Similarly, the capacity of the yarn was set to

$$F = \eta_F F_0 \tag{9}$$

where F_0 is the yarn capacity reported by the manufacturer (Table 1), and the efficiency factor for the strength η_F was set to 34 % according to earlier pull-out tests and calibration [27]. The material model of the yarn is linear elastic up until the maximum force $\eta_F F_0$ is reached, after which the simulation is terminated.

For the interface, a similar bond-slip model as presented for traditional rebars in fib Model Code [51] was used. The model considers an initially nonlinear development of bond stress upon increasing slip, reaching a plateau at the maximum value of the bond stress. After the plateau, the stress decreases linearly until a final plateau is reached, see Fig. 5. In total, the model formulation requires 7 parameters. Among those, four are slip values s_0 - s_3, and two are bond stress values τ_{max} and τ_f for the maximum and final bond stress, respectively. The last parameter, α, describes the nonlinear growth in the first segment as

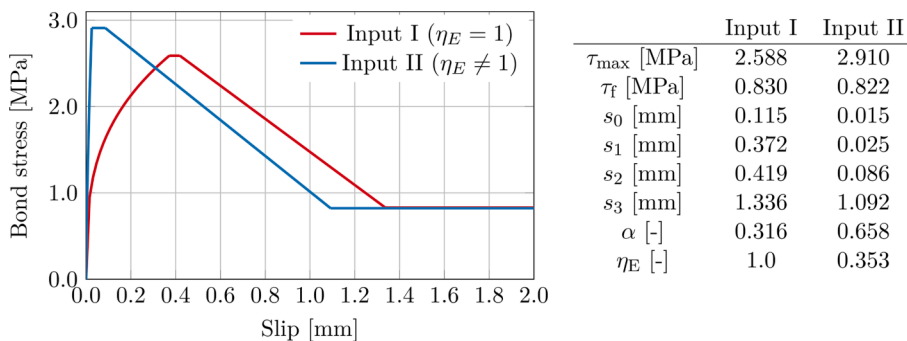|	Input I	Input II
$\tau_{\max}$ [MPa]	2.588	2.910
τ_{f} [MPa]	0.830	0.822
s_0 [mm]	0.115	0.015
s_1 [mm]	0.372	0.025
s_2 [mm]	0.419	0.086
s_3 [mm]	1.336	1.092
α [-]	0.316	0.658
η_{E} [-]	1.0	0.353

Fig. 6. Bond stress versus slip used as input, results of the calibration procedure from [38].

$$\tau(s) = \tau_{\max} \left(\frac{s}{s_1} \right)^{\alpha} \qquad (10)$$

It is noteworthy, that the parameter s_0 is not included in [51], but is used in the software implementation. For numerical performance, a linear stiffness of the interface is considered for slip values up to the initial slip of s_0.

As already alluded to, two sets of input parameters were chosen. The main difference between them were whether the efficiency factor for stiffness,η_E, was set to 1.0 or a calibrated value. However, also the bond-slip response varied in the different inputs; as its calibration in [38] depended on the assumedη_E. Thus, the two input sets were defined by:

- *Input I (η_E=1):* The efficiency factor for the stiffness,η_E, was set to 1.0, and the bond-slip relation calibrated with this assumption was used.
- *Input II ($\eta_E \neq 1$):* The efficiency factor for the stiffness,η_E, was set to its calibrated value of 0.353, and the bond-slip relation from the same calibration procedure was used.

The bond-slip relation for both input sets can be seen in Fig. 6.

3.3. Numerical simulations

3.3.1. General

In tensile and one-way flexure (T- and O-series) analyses, quadrilateral 4-node plane stress elements based on bi-linear interpolation with a side length of 2 mm were used for the concrete solid, whereas a side length of 2.5 mm was used in analyses of deep beams (D-series). For the textile reinforcement, 2-node truss elements (with the same size as the corresponding concrete elements) were used. Between the constituents, interface elements with linear shape functions were generated by the software.

The analyses were run in displacement control, until a prescribed displacement was reached. For the equilibrium iterations, the Newton-Raphson method was used, and the relative convergence tolerance was set to 0.01 for both the iterative displacement increment and out-of-balance force norms. In practice, the simulations were run until failure of convergence, which corresponded to ultimate failure of the specimen. In addition to choosing a suitable crack band width (equal to the element length), mesh independence was assured with a convergence analysis (with respect to element size) in terms of the value of the first peak/cracking load. For each input set and test type, ten realisations were analysed with randomised distribution of the concrete properties at the positions of the transverse yarns.

3.3.2. Model of the uniaxial tensile test

The uniaxial tensile tests (*T*-series) were modelled in two-dimensions assuming plane stress, with the thickness of the concrete solid equal to 8 mm. Due to presence of the machine clamps, only a 300 mm long strip of the panel was modelled, so that seven openings fit within the measuring range (based on the measurements of the mesh in Table 1, the centre-
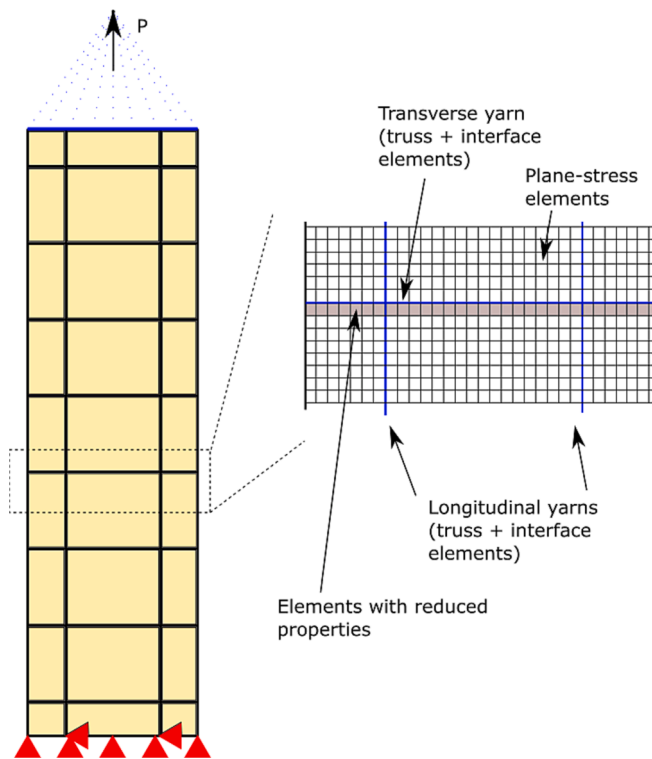

Fig. 7. Schematic view of the finite element model of the uniaxial tensile tests with boundary conditions and prescribed deformation. Tensile strength, fracture energy, and Young's modulus of the elements adjacent to transverse yarns were sampled according to Eqs. (5)–(7).

centre yarn spacing was equal to 37.5 mm). The textile reinforcement mesh was placed as in the experiments. Corresponding with the yarn's measured average width and thickness (Table 1), a cross-section area of 1.367 mm^2 and a perimeter of 7.872 mm were assigned to each yarn.

The restraint from the testing machine was simulated by constraining the vertical displacements of all the nodes at the bottom edge (including the yarn displacements). The vertical displacement of all the nodes, concrete and yarn, at the top edge was tied (equally) to the vertical displacement of a dummy master node, see Fig. 7. The experiment was then simulated by prescribing a vertical displacement to this master node.

As described in Section 3.2, a reduction factor ζ was introduced for the material properties of the concrete at the position of the transverse yarns. Starting from the conservation of the cross-sectional area of the element row highlighted in Fig. 7, we see that the nominal cross-sectional area can be expressed as $h_c t_c$, where h_c is the element length and t_c is the thickness of the specimen. Accounting for the cross-sectional
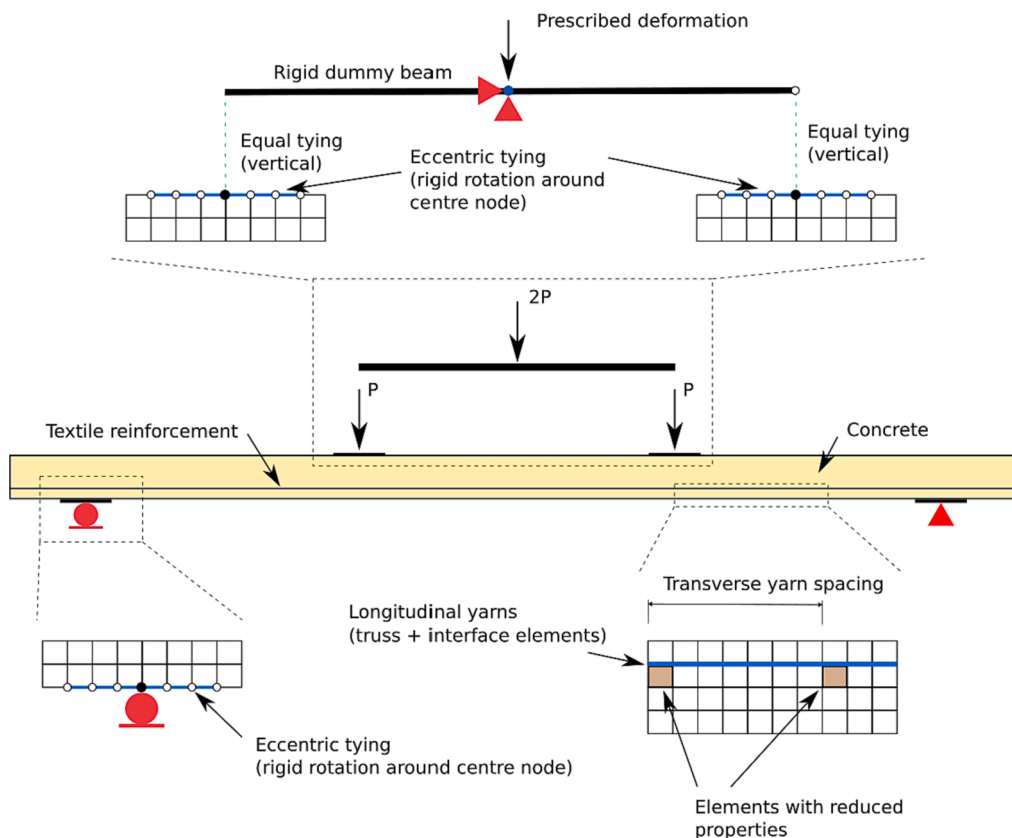
Fig. 8. Schematic view of the finite element model of the one-way flexure tests along with boundary conditions and prescribed deformation. Tensile strength, fracture energy, and Young's modulus of the elements at the location of transverse yarns were sampled according to Eqs. (5)–(7).

area of the yarn, A_f, the modified thickness of the element row can be calculated as $t_c - \frac{A_f}{h_c}$ so that the total volume is conserved. The ratio of the modified and nominal thickness gives the final reduction factor. Thus, for the *T*-series, it was determined as:

$$\zeta = \zeta_T = 1 - \frac{A_f}{h_c t_c}, \tag{11}$$

and was calculated to be 0.914 for the chosen mesh.

To compute the force versus deformation response, the total force was obtained as the vertical reaction force in the master node, whereas the deformation was obtained as the vertical displacement of the same node. Similarly, the crack widths were extracted from the model as the difference in vertical displacement of the nodes at opposite sides of each crack.

3.3.3. Model of the one-way flexure test

The specimen in the one-way flexure test (O-series) was modelled in plane stress with the length of 900 mm and the height of 20 mm. A schematic view of the model can be seen in Fig. 8. A thickness of 200 mm was assigned to the concrete, representing the complete test specimen. For the textiles, only the longitudinal yarns were modelled. In the experiments, there were, in total, 5 longitudinal yarns over the thickness (see Fig. 2); accordingly, the reinforcement in the model was defined with a cross-section and perimeter of 6.835 mm^2 and 39.36 mm (5 times the area and perimeter of a single yarn), respectively.

The nodes close to supports and point loads were tied eccentrically. This allowed for rigid body rotation of the edge around the master nodes, which were chosen at the centre of the supports and point loads. To run the simulation in displacement control, it was necessary to define a rigid dummy beam, which ends were tied to the beam (see Fig. 8). By doing this, it was possible to prescribe a vertical displacement in a single

master node (in the middle of the rigid dummy beam). In this way, the load was divided equally to both loading points of the beam, simulating the real experiment. The total force was obtained as the vertical reaction force in the master node at the rigid dummy beam, and the mid-span deflection was computed according to Fig. 3.

In order to mimic the presence of the transverse textile yarns and to trigger cracking, material properties of evenly spaced elements (with spacing of 37.5 mm) at the level of the longitudinal yarn (see Fig. 8) were sampled according to Eqs. (5)–(7).

Regarding the reduction factor ζ, similar argument as for the *T*-series can be used to calculate the modified thickness of the highlighted element row as $t_c - \frac{A_f t_c}{h_c^2}$ for the *O*-series. Thereby, the reduction factor for the *O*-series model can be determined as:

$$\zeta = \zeta_O = 1 - \frac{A_f}{h_c^2}, \tag{12}$$

where A_f is the cross-sectional area of the transverse yarn, and h_c is the size of the concrete element. For the chosen mesh, ζ_O was calculated to be 0.658.

3.3.4. Model of the deep beam

For the D-series, each specimen was modelled as a two-dimensional deep beam in plane stress with the length of 900 mm and the height of 200 mm. A thickness of 20 mm was assigned to the concrete. For the textile reinforcement grid, both the longitudinal and transverse yarns were modelled. The reinforcement in both longitudinal and transverse direction was modelled with the corresponding cross-section area and perimeter of 4.101 mm^2 and 23.634 mm (3 times the area and perimeter of a single yarn, as there were 3 layers of reinforcement over the thickness in the experiments, see Fig. 4), respectively. A schematic view of the model can be seen in Fig. 9.
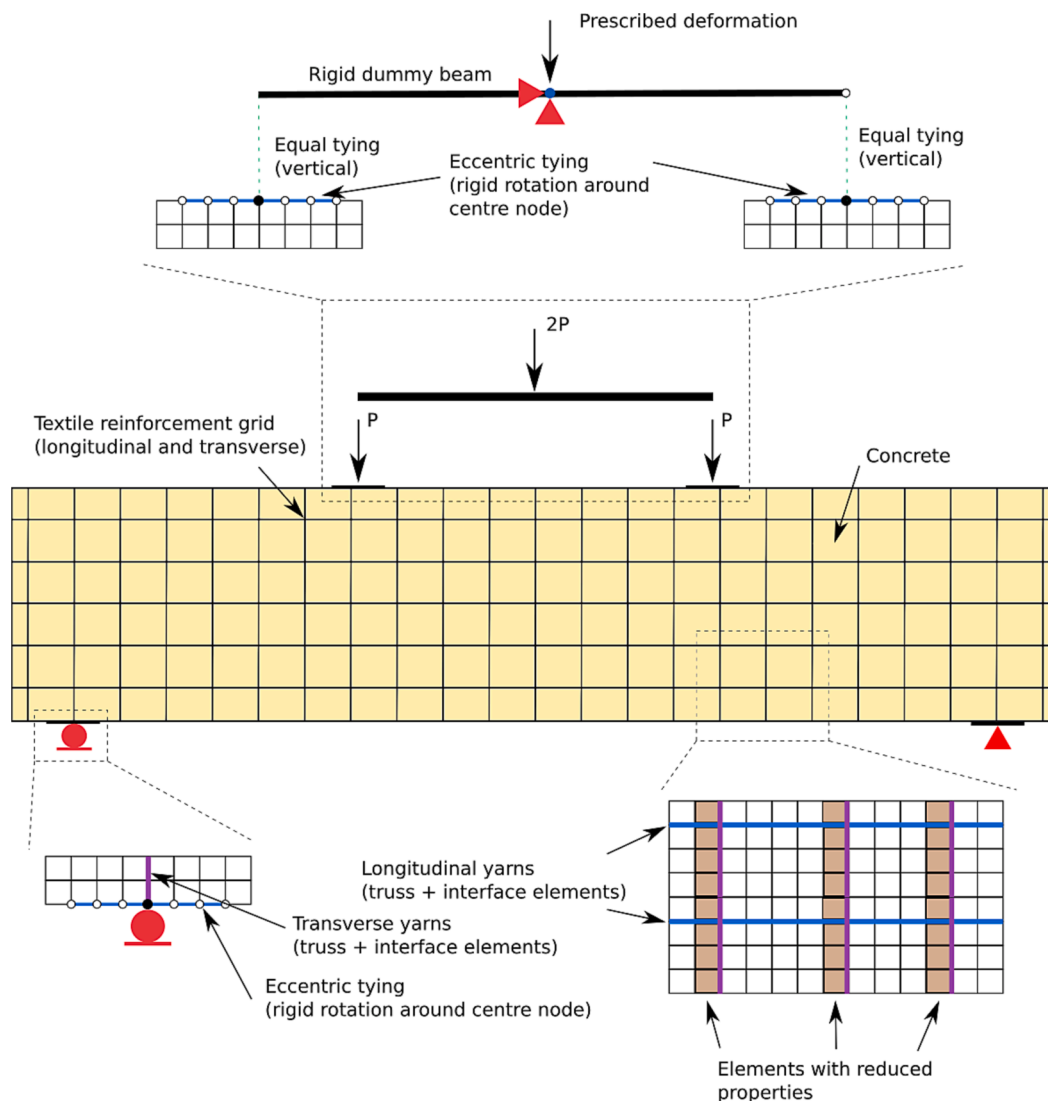
Fig. 9. Schematic view of the finite element model of deep beams along with boundary conditions and prescribed deformation. Tensile strength, fracture energy, and Young's modulus of the elements adjacent to transverse yarns were sampled according to Eqs. (5)–(7).

As in the *O*-series model, the nodes close to supports and point loads were tied eccentrically, to simulate support and loading plates. Similarly, a rigid dummy beam was used to control the loading process with a single master node.

In order to trigger localization (cracking), material properties of elements adjacent to transverse yarns (see Fig. 9) were sampled according to Eqs. (5)–(7). For the *D*-series model, the corresponding reduction factor was determined identically as for *T*-series model as:

$$\zeta = \zeta_D = 1 - \frac{A_f}{h_c t_c}, \tag{13}$$

where A_f is the cross-sectional area of the transverse yarn, t_c is the thickness of the concrete elements, and h_c is the size of the concrete element. For the chosen mesh, ζ_D was calculated to be 0.918.
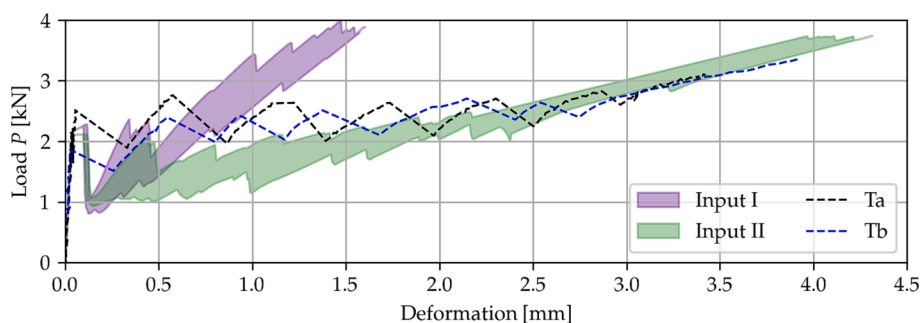

Fig. 10. Load (*P* as defined in Fig. 7) versus deformation for uniaxial tensile tests and analyses. Shaded areas indicate the spread of the random numerical realisations, while the dashed lines show the experimental results.
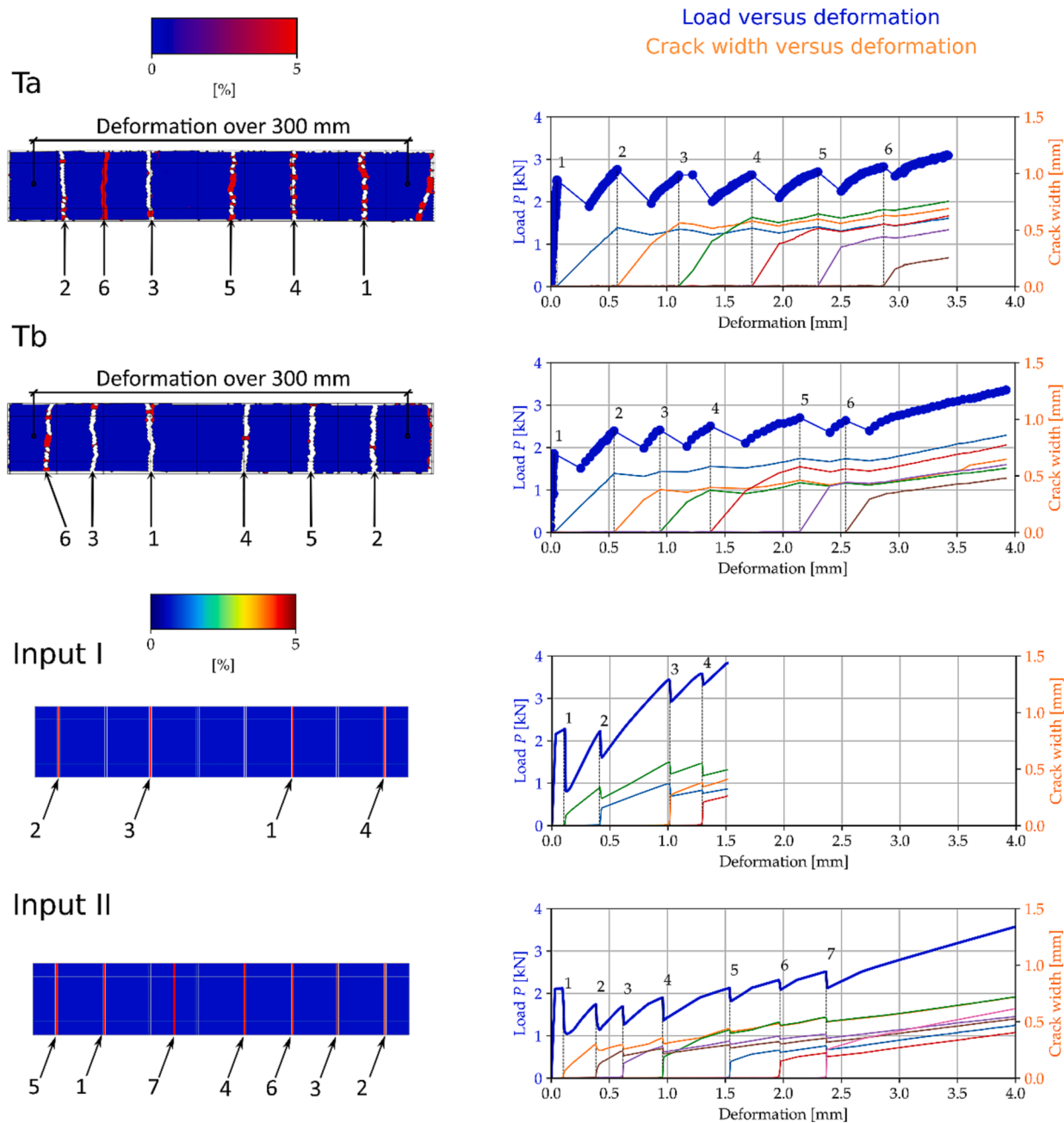
Fig. 11. Experimental (*Ta* and *Tb*) and numerical (*Input I* and *Input II*) results of uniaxial tension tests. Left: Contour plots of the main principal strain at maximum load (*P* as defined in Fig. 7). The placement of the textile mesh is indicated. Cracks are numbered in order of appearance. Right: Load and crack widths versus deformation over the 300 mm long measuring range.

The total force was obtained as the vertical reaction force in the master node at the rigid dummy beam, and the mid-span deflection was computed according to Fig. 3.

4. Results and discussion

4.1. Uniaxial tensile tests and analyses

For the tensile tests, two specimens were considered, named *Ta* and *Tb* according to Section 2.1. Starting with the global response, external load versus deformation for all uniaxial tensile tests and the corresponding numerical analyses is presented in Fig. 10. In the figure, the scatter in the numerical realisations is indicated by the shaded areas. The initial cracking load agreed reasonably well for both sets of input,

and the maximum load and deformation at failure was captured well by Input II. After initial cracking, subsequent cracks formed at approximately the same load level as the initial crack; this behaviour was observed both in experiments and in analyses regardless of the input set. The overall observed stiffness was much higher for Input I, where failure took place at a deformation of around 1.5 mm. In the analyses with Input II, a deformation of around 4 mm was reached before failure, agreeing well with the experimentally observed.

Both uniaxial tests showed a very similar behaviour, see Fig. 11. Cracking transverse to the loading direction took place, starting at relatively low load levels with increasing number of cracks for increasing load. The first crack always appeared at a crossing yarn, so did also most of the later cracks. In one specimen, *Ta*, the first two cracks appeared outside the measuring range; one of these is visible in Fig. 11
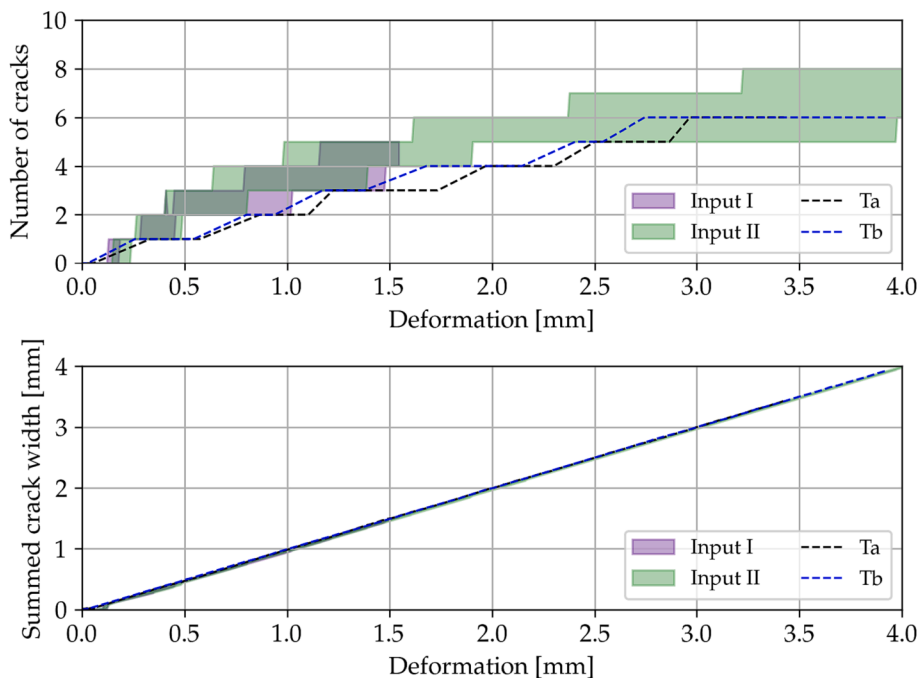
Fig. 12. Detailed crack information for uniaxial tensile tests and analyses. Top: number of open cracks versus deformation. Bottom: summed crack width versus deformation.
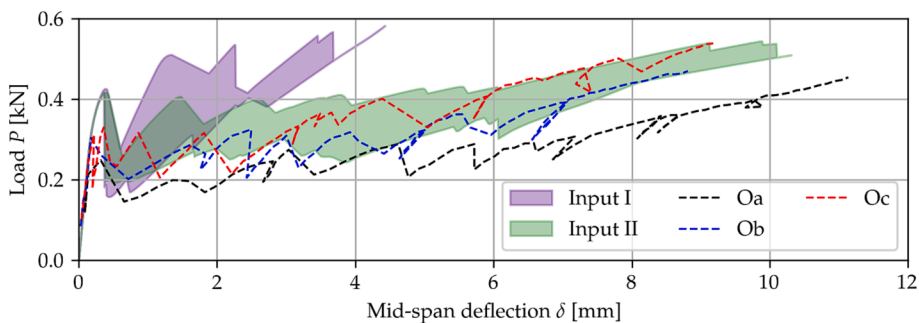

Fig. 13. Load (*P* as defined in Fig. 8) versus mid-span deflection for the one-way flexure tests and analyses.

but they are not given any crack numbers as the results focus on the measuring range. At higher loads, smaller cracks along the yarns in the loading direction were also visible. Failure took place by rupture of the yarns at a cross-thread.

Corresponding results from the finite element analyses, from one realisation selected to be representative for each set of input parameters, can be seen in the lower part of Fig. 11. In the analysis applying Input I, only four cracks were observed before the textile yarns failed in rupture. In contrast, seven cracks formed before failure for Input II, which agrees better with the experimental results. The individual crack widths in the simulation applying Input II were also in agreement with the experimental results, with the majority of the cracks growing to widths around 0.5 mm.

In order to investigate the cracking process further, the number of cracks and the total (summed) crack width are presented in Fig. 12, where the shaded regions indicate the spread of the simulations with randomised material parameters. From the figure, it is evident that the number of cracks agrees well with experiments when *Input II* is applied, although the number of cracks depends on the realisation (with the possibility of having either fewer or more cracks than in the experiment). The total summed crack width is almost identical with the deformation in both experiments and numerical simulations, with almost no visible scatter. This is an expected result as uniaxial tension is

studied; it means that all deformation is taken in the cracks, and that the deformation between the cracks is negligible. It should be noted, though, that the results from analyses with *Input I* end at a deformation around 1.5 mm; this is difficult to see in Fig. 12 (bottom) but can be seen in Fig. 10 and Fig. 12 (top).

4.2. One-way flexure tests and analyses

Experimental (*Oa*, *Ob*, and *Oc* tests according to Section 2.1) and numerical load–deflection results of the one-way flexure tests are shown together in Fig. 13, with the shaded regions indicating the spread of the random numerical realisations. Although the initial cracking load was overestimated in the analyses for both input sets, the maximum load and deflection at failure was captured reasonably well by *Input II*. The overall observed stiffness was much higher in the analyses applying *Input I*, where failure took place at a mid-span deflection of around 3.5 mm. In the analyses applying *Input II*, a deflection of around 10 mm was reached before failure, agreeing well with experimental observations. It is noteworthy that the scatter of experimental results is larger than in the previously described test type (*T*-series). A possible explanation may be that this test setup is very sensitive to small deviations in the placement of the reinforcement mesh, as that directly influences the inner lever arm and thereby the bending capacity. No such variation was applied in the
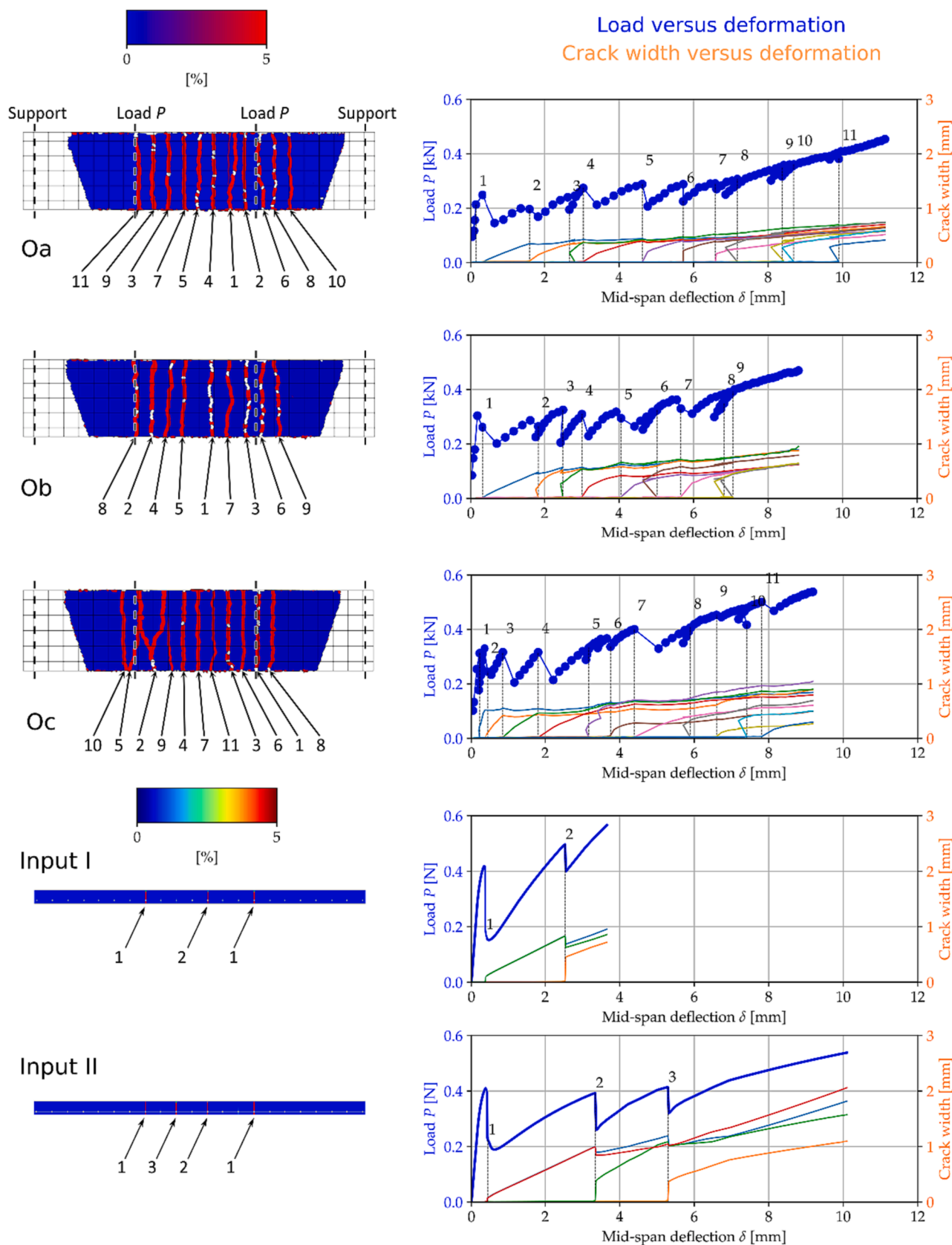
Fig. 14. Experimental (*Oa*, *Ob*, *Oc*) and numerical (*Input I* and *Input II*) results of one-way flexure tests. Left: Contour plots of the main principal strain at maximum load (*P* as defined in Fig. 8). The placement of the textile mesh is indicated. Cracks are numbered in order of appearance. Right: Load and crack widths versus mid-span deflection relative to the deflection at the load positions, see Fig. 3.
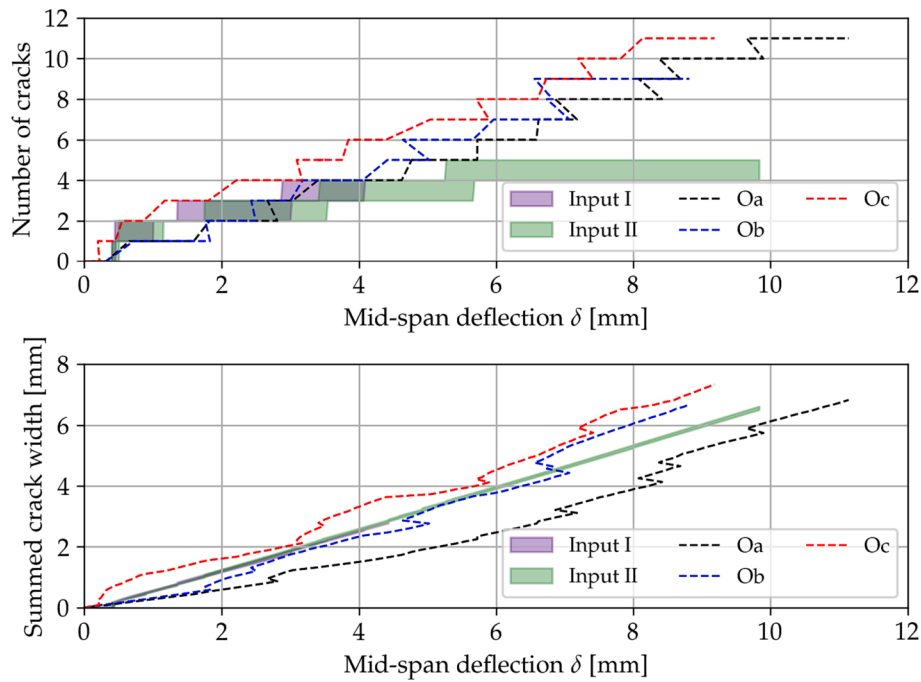
Fig. 15. Detailed crack information for the one-way flexure tests and analyses. Top: number of open cracks versus deflection. Bottom: summed crack width versus deflection.

numerical realisations.

The experimental results of the one-way flexure tests are shown in the top part of Fig. 14. After an initial stiff behaviour, cracking took place, first in the region between the loads, and for higher loads also between the loads and the supports. It can be noted that cracking preferably took place at the transverse yarns, and in later stages, one crack appeared at each transverse yarn in the mid part of the slab. Rupture of the longitudinal yarns limited the maximum load, without any visible slip between the yarns and the concrete.

Corresponding results from finite element realisations selected to be representative can be seen in the bottom part of Fig. 14. In contrast to experiments (where a view from the bottom is used to show the cracks), the specimens are shown from the side. The crack widths were computed as the difference in horizontal deformation on both sides of the crack, at the tensioned side of the slab. Three and four cracks were observed before the textile yarns failed in rupture, in the analyses with *Input I* and *II,* respectively. Thus, fewer cracks were obtained in the analyses than in the experiments. Further, larger crack widths appeared in the analyses than in the experiments. It can also be noted that in the analyses, sometimes two cracks appeared simultaneously, which contrasts the experimental results where one crack at a time was observed. This difference, together with the fewer cracks in the analyses, explains the lower number of local peaks in the load–displacement diagram from the

simulations.

As already mentioned, the initial cracking load was overestimated in the analyses for both input sets compared to the experimental results. By looking more into detail in the results around this first peak in the analysis, it was clear that there were issues for the first crack to localise. The load that can be calculated from beam theory and tensile strength (0.23 kN) agrees well with the cracking load in the experiments. Cracking did indeed take place at this load in the simulations, but the load could be further increased while cracking spread to several neighbouring elements. The localisation could be forced to take place for a lower load by exaggerating the reduction factor; however, instead of choosing an ad-hoc value, it was chosen to use the value motivated from the conservation of volume according to Eq. (12). Increasing the variance in the assumed Gaussian distribution of the material parameters may also have triggered first localisation in a better way. Another possible reason to this localisation issue can be that the applied constitutive model for concrete in tension (Hordijk et al. [53]) may overestimate the capacity directly after cracking.

To explore the cracking behaviour further, the number of cracks and the total (summed) crack width are presented in Fig. 15. As mentioned, the analyses resulted in fewer but larger cracks than the experiments. Still, the sum of the crack widths produced by *Input II* agreed very well with the experiments. Similar as for the uniaxial tension test series, the
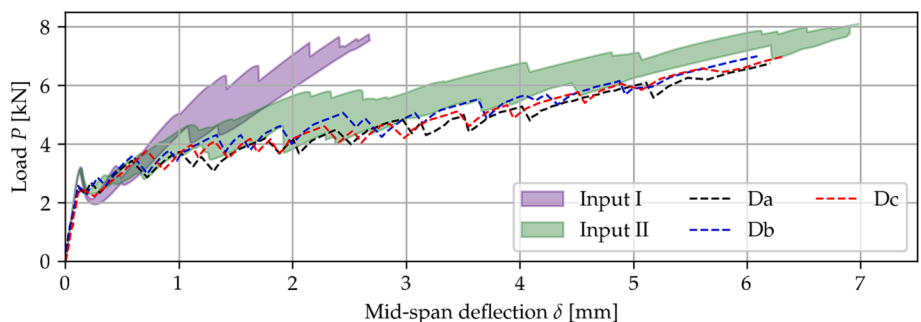

Fig. 16. Load (P as defined in Fig. 9) versus mid-span deflection for the tests and analyses of deep beams.
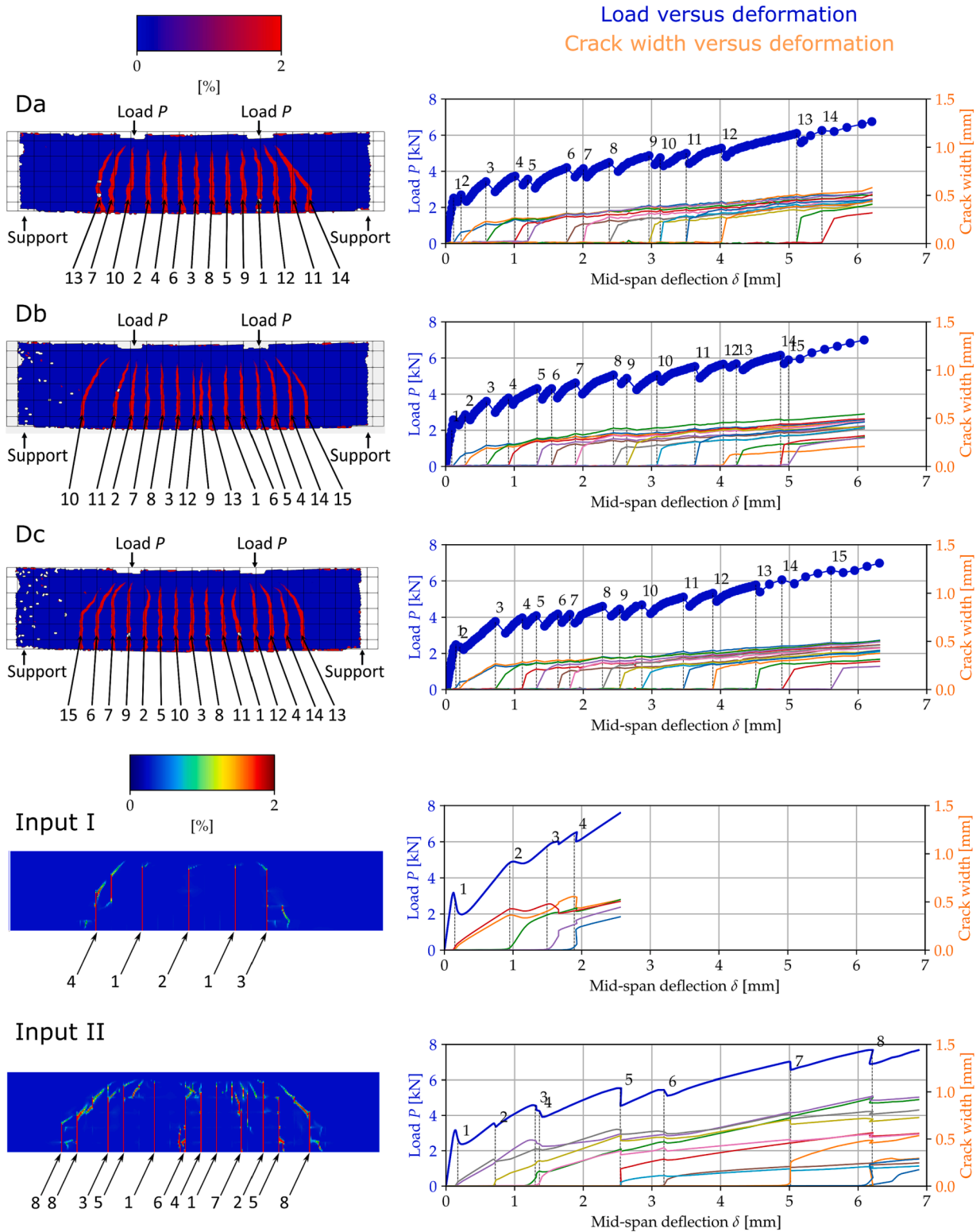
Fig. 17. Experimental (*Da*, *Db*, *Dc*) and numerical (*Input I* and *Input II*) results of tests on deep beams. Left: Contour plots of the main principal strain at maximum load (*P* as defined in Fig. 9). The placement of the textile mesh is indicated. Cracks are numbered in order of appearance. Right: Load and crack widths versus mid-span deflection.

numerical spread of the total crack width due to material randomness is negligible.

4.3. Tests and analyses of deep beams

Experimental (*Da*, *Db*, and *Dc* tests according to Section 2.1) and numerical load–deflection results for the tests and analyses of deep beams are shown together in Fig. 16, where the shaded regions indicate
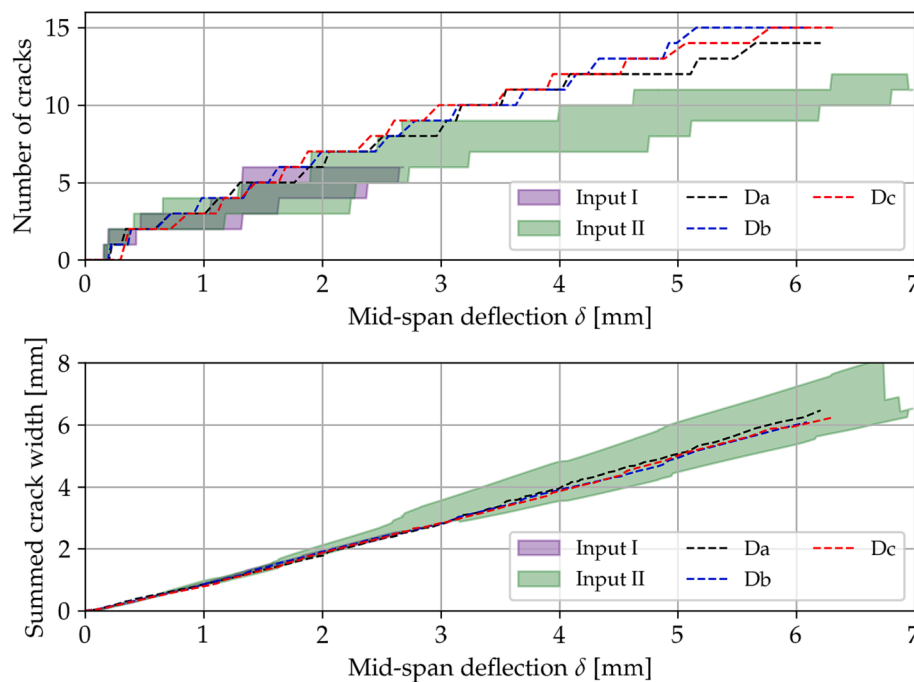
Fig. 18. Detailed crack information from tests and analyses of deep beams. Top: number of open cracks versus deformation. Bottom: summed crack width versus deformation.

the spread due to the random realisations in the analyses. The initial cracking load in the analyses agreed reasonably well with the experiments, although slightly overestimated. Similarly, the maximum load and deflection at failure in the analyses with *Input II* were also agreeing reasonably well with experimental results, with a slight overestimation in the analyses. Failure with rupture of the yarn took place, both in experiments and analyses. The overall observed stiffness was much higher in the analyses with *Input I*, which had a deflection of around 2.5 mm at failure. This can be compared to a deflection around 6 to 7 mm in experiments and simulations with *Input II*.

The load versus mid-span deflection from the experiments of deep beams is shown in the top part of Fig. 17. The average maximum load was 6.9 kN, ranging from 6.75 kN to 7.0 kN. In all three tests, the general behaviour was the same: The first bending cracks appeared between the loading points at loads of about 2.5 kN, after which several more bending cracks appeared for increasing load. The first cracks started from the bottom edge and gradually grew over the height of the beam. At loads between 3.5 and 6 kN, more cracks between the point loads appeared; these cracks typically appeared all over their height instantaneously. At load levels between 4 and 5 kN, cracks also appeared in the shear spans, but still close to the point load positions. At higher load levels, of about 5.5 to 6 kN, inclined cracks appeared in the shear span. Finally, failure took place in the zone between the point loads, with large opening of one of the bending cracks and rupture of the yarns in the bottom part of the beam. At failure, smaller cracks along the loaded yarns close to the opening crack also appeared; likely because slip occurred along the loaded yarns at failure. The failure was very brittle, and the remaining load capacity after failure was very small.

Corresponding results from one finite element realisation selected to be representative for each input set are shown in the lower part of Fig. 17. The crack width of individual cracks was evaluated from the displacement between two points along a line situated 25 mm above the bottom of the deep beam, in a similar manner as the crack widths from experiments. For *Input I*, only five cracks were observed before the textile yarns failed in rupture. In contrast, twelve cracks formed before failure for *Input II*. Similar as in the experimental results, individual cracks are associated with local peaks in the load–deflection diagram.

Contrary to the tests, two or more cracks often appeared simultaneously in the analyses, as can be seen in Fig. 17. The first cracks appeared in the mid-region of the beam, with some distance between them. Later, cracks appeared both in between already existing cracks in the mid-region of the beam, as well as closer to supports. The individual crack widths varied more in the analyses than in the experiments, but the average crack width at failure (around 0.5 mm) agreed rather well, regardless of the input set.

To explore the cracking behaviour further, the number of cracks and the total (summed) crack width are presented in Fig. 18. Similar as for the one-way slab series, the analyses have slightly fewer cracks than the experiments. The sum of the crack widths in analyses with *Input II* agreed very well with the experiments, reaching a value of around 6 mm at failure. In the analyses of the deep beams, there is a noticeable spread of the summed crack width in the analyses, and the experimental results seem to be contained within it.

5. Conclusions and outlook

In this work, experiments of TRC specimens were carried out, using both common test setups such as uniaxial tension and one-way slab tests, and a novel test setup of deep beams including a more complex load situation. Further, nonlinear FE analyses of the specimens were carried out, applying an earlier calibrated bond-slip relation and efficiency factors for strength and stiffness of the textile reinforcement. The aim was to investigate how well the behaviour can be predicted by such analyses, especially for the complex load situations. The following conclusions can be drawn:

- By applying the parameters obtained from the calibration procedure suggested earlier, the structural behaviour of TRC could be described well in analyses, not only for specimens subjected to primarily uniaxial loading but also for a more complex loading case including in-plane bending and shear. This statement is true when the calibrated bond-slip input including a calibrated efficiency factor for the stiffness of the yarn was applied. In these analyses, the overall stiffness, ultimate load and deformation, number of cracks, and total
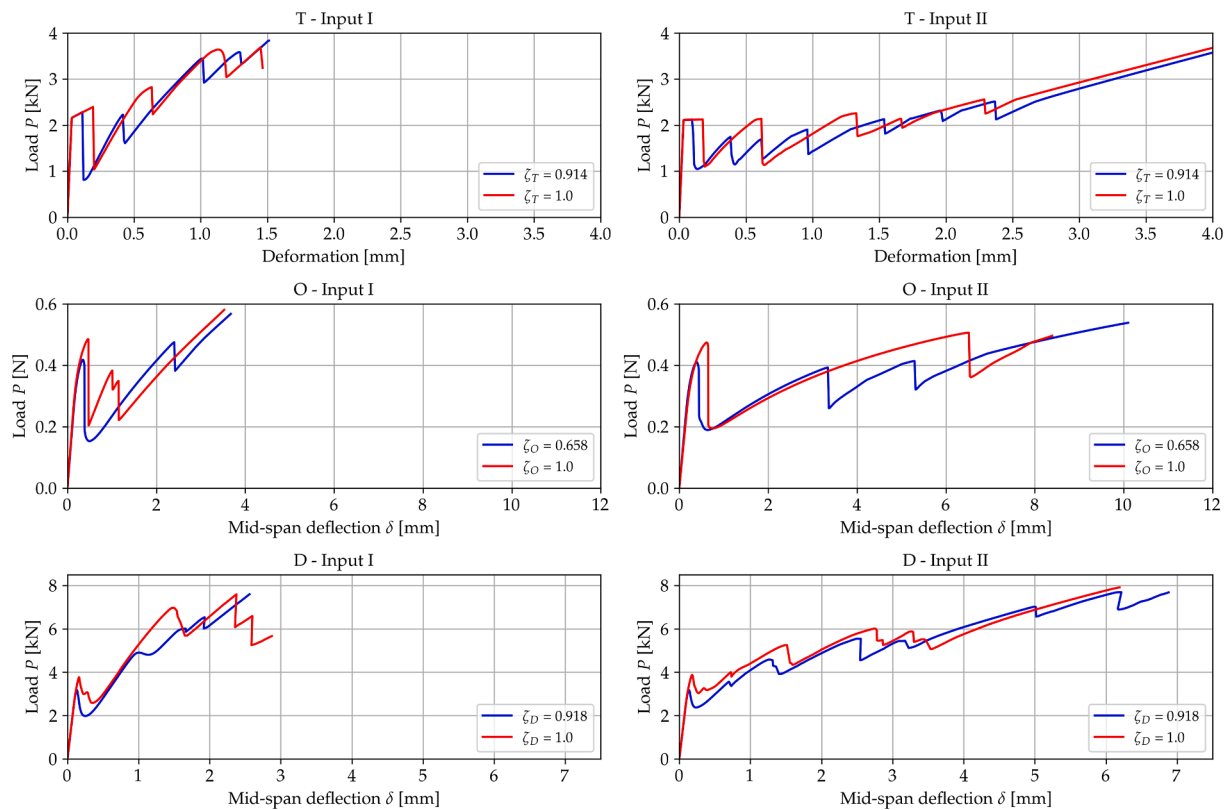
Fig. A1. Comparison of the load-deformation results for the same random realizations modelled with and without the reduction factors $\zeta_T, \zeta_O, \zeta_D$.

(summed) crack width, could be described with reasonably good accuracy. On the other hand, when the efficiency factor for the stiffness of the yarn was set to 1.0, the analyses typically showed too stiff behaviour compared to experiments. Thus, the inclusion of a calibrated efficiency factor for the stiffness of the yarn was shown to be vital. The analyses including a calibrated efficiency factor for the stiffness of the yarn are in focus in the remainder of the conclusions.

- The material properties of the concrete at the location of transverse yarns were randomised and weakened to account for the volume of the concrete in the (weakened) element row being effectively smaller due to the presence of the transverse yarn. These remedies were done to trigger strain localisation and were shown to ensure cracks to appear at the transverse yarns in the analyses, in a similar manner as in experiments. Still, the initial cracking load in bending was over-estimated because of problems for the first crack to localise.
- In the analyses describing bending behaviour, both one-way slabs and deep beams, the number of cracks was slightly underestimated, and individual crack widths slightly overestimated when comparing with experimental results. Further, the variation in width of individual cracks was larger in analyses than in experiments.
- The more complex the loading situation was, the larger the spread of total crack width in different randomised numerical realisations.

For future work on analyses of TRC, it is recommended to include efficiency factors for both the stiffness and the strength of the yarn, together with calibrated bond-slip relation describing the interaction between yarn and concrete, and to weaken and randomise the material properties of the concrete at the location of transverse yarns to trigger cracking. Due to the relatively small scale of the textile reinforcement grid (compared to conventional steel reinforcement), multiscale numerical procedures should preferably be developed to analyse large scale structures efficiently, omitting the need to resolve every single yarn.

CRediT authorship contribution statement

Adam Sciegaj: Formal analysis, Investigation, Software, Visualization, Writing – original draft, Writing – review & editing, Methodology, Validation. **Sebastian Almfeldt:** Data curation, Investigation, Methodology, Visualization, Resources. **Fredrik Larsson:** Conceptualization, Investigation, Methodology, Writing – review & editing, Validation. **Karin Lundgren:** Conceptualization, Funding acquisition, Investigation, Methodology, Project administration, Resources, Writing – original draft, Writing – review & editing, Validation.

Declaration of Competing Interest

The authors declare that they have no known competing financial interests or personal relationships that could have appeared to influence the work reported in this paper.

Data availability

Data will be made available on request.

Acknowledgements

Appendix A. Influence of the reduction factor ζ

In this Appendix, the influence of the reduction factors $\zeta_T, \zeta_O, \zeta_D$ on the structural load-deformation response is briefly discussed. As already presented in Section 3, the reduction factor is defined as the ratio of the modified and nominal thickness of the model. The modified thickness can be calculated from the conservation of the volume in a part of the model when accounting for the presence textile reinforcement. It is then effectively used to reduce the stiffness, strength and fracture energy of concrete to properly trigger localization. To show the effect of using the reduction factors, one random realisation of each model was analysed without applying the factor, i.e., setting it equal to 1. The results are illustrated in Fig. A1.

The biggest impact of the reduction factor can be seen for one-way flexure and deep beam tests (*O*- and *D*-series), i.e., where cracks grew progressively instead of localising within an entire element row at once (which occurred in the *T*-series). If no reduction factor is used, the first peak/cracking load tended to be higher than the one found in experimental tests. This effect was not present in *T*-series models, as each crack localised in the full width of the model. Moreover, fewer cracks tended to form in all models (also for *T*-series models) compared to the experiments when no reduction factor was used.

References

[1] L.N. Koutas, T. Zoi, D.A. Bournas, T.C. Triantafillou, Strengthening of concrete structures with textile reinforced mortars: state-of-the-art review, J. Compos. Constr. 23 (1) (2019), 03118001, https://doi.org/10.1061/(ASCE)CC.1943-5614.0000882.

[2] J. Hegger, C. Kulas, M. Horstmann, Realization of TRC façades with impregnated AR-glass textiles, Key Eng. Mater. 466 (2011) 121–130, https://doi.org/10.4028/www.scientific.net/KEM.466.121.

[3] T. Helbig, K. Unterer, C. Kulas, S. Rempel, J. Hegger, Fuß- und radwegbrücke aus carbonbeton in albstadt-ebingen, Beton- Stahlbetonbau 111 (10) (2016) 676–685, https://doi.org/10.1002/best.201600058.

[4] S. Rempel, C. Kulas, N. Will, J. Bielak, Extremely LIGHT AND SLENDER PRECAST PEDESTRIAN-BRIDGE MADE OUT OF TEXTILE-REINFORCED CONCREte (TRC), in: D.A. Hordijk, M. Luković (Eds.), High Tech Concrete: Where Technology and Engineering Meet, Springer International Publishing, Cham, 2018, pp. 2530–2537.

[5] P. Preinstorfer, B. Kromoser, J. Kollegger, Flexural behaviour of filigree slab elements made of carbon reinforced UHPC, Constr. Build. Mater. 199 (2019) 416–423, https://doi.org/10.1016/j.conbuildmat.2018.12.027.

[6] W. Hawkins, J. Orr, T. Ibell, P. Shepherd, A design methodology to reduce the embodied carbon of concrete buildings using thin-shell floors, Eng. Struct. 207 (2020), 110195, https://doi.org/10.1016/j.engstruct.2020.110195.

[7] S. May, O. Steinbock, H. Michler, M. Curbach, Precast slab structures made of carbon reinforced concrete, Structures 18 (2019) 20–27, https://doi.org/10.1016/j.istruc.2018.11.005.

[8] A. Schumann, H. Michler, F. Schladitz, M. Curbach, Parking slabs made of carbon reinforced concrete, Struct. Concr. 19 (3) (2018) 647–655, https://doi.org/10.1002/suco.201700147.

[9] J. Hegger, M. Curbach, A. Stark, S. Wilhelm, K. Farwig, Innovative design concepts: application of textile reinforced concrete to shell structures, Struct. Concr. 19 (3) (2018) 637–646, https://doi.org/10.1002/suco.201700157.

[10] A. Scholzen, R. Chudoba, J. Hegger, Thin-walled shell structures made of textile-reinforced concrete. Part II: experimental characterization, ultimate limit state assessment and numerical simulation, Struct. Concr. 16 (1) (2015) 115–124, https://doi.org/10.1002/suco.201400046.

[11] A. Scholzen, R. Chudoba, J. Hegger, Thin-walled shell structures made of textile-reinforced concrete. Part I: structural design and construction, Struct. Concr. 16 (1) (2015) 106–114, https://doi.org/10.1002/suco.201300071.

[12] B. Banholzer, Bond of a strand in a cementitious matrix, Mater. Struct. 39 (10) (2006) 1015–1028, https://doi.org/10.1617/s11527-006-9115-y.

[13] E. Lorenz and R. Ortlepp, "Bond Behavior of Textile Reinforcements - Development of a Pull-Out Test and Modeling of the Respective Bond versus Slip Relation," in *High Performance Fiber Reinforced Cement Composites 6: HPFRCC 6*, G. J. Parra-Montesinos, H. W. Reinhardt, and A. E. Naaman, Eds., Dordrecht: Springer Netherlands, 2012, 479–486. 10.1007/978-94-007-2436-5_58.

[14] J. Butler, V. Mechtcherine, S. Hempel, Experimental investigations on the durability of fibre–matrix interfaces in textile-reinforced concrete, Cem. Concr. Compos. 31 (4) (2009) 221–231, https://doi.org/10.1016/j.cemconcomp.2009.02.005.

[15] Y. Li, J. Bielak, J. Hegger, R. Chudoba, An incremental inverse analysis procedure for identification of bond-slip laws in composites applied to textile reinforced concrete, Compos. B Eng. 137 (2018) 111–122, https://doi.org/10.1016/j.compositesb.2017.11.014.

[16] N. Williams Portal, I. Fernandez Perez, L. Nyholm Thrane, K. Lundgren, Pull-out of textile reinforcement in concrete, Constr. Build. Mater. 71 (2014) 63–71, https://doi.org/10.1016/j.conbuildmat.2014.08.014.

[17] R. T. C. 232-T. Wolfgang Brameshuber, "Recommendation of RILEM TC 232-TDT: test methods and design of textile reinforced concrete," *Mater Struct*, 49, 12, 4923–4927, 2016, 10.1617/s11527-016-0839-z.

[18] N. Williams Portal, M. Flansbjer, P. Johannesson, K. Malaga, K. Lundgren, "Tensile behaviour of textile reinforcement under accelerated ageing conditions", journal of building, Engineering 5 (2016) 57–66, https://doi.org/10.1016/j.jobe.2015.11.006.

[19] J. Hartig, F. Jesse, K. Schicktanz, U. Häußler-Combe, Influence of experimental setups on the apparent uniaxial tensile load-bearing capacity of textile reinforced concrete specimens, Mater. Struct. 45 (3) (2012) 433–446, https://doi.org/10.1617/s11527-011-9775-0.

[20] M. Lee, J. Mata-Falcón, W. Kaufmann, Load-deformation behaviour of weft-knitted textile reinforced concrete in uniaxial tension, Mater. Struct. 54 (6) (2021) 210, https://doi.org/10.1617/s11527-021-01797-5.

[21] S.V. Lomov, et al., Experimental methodology of study of damage initiation and development in textile composites in uniaxial tensile test, Compos. Sci. Technol. 68 (12) (2008) 2340–2349, https://doi.org/10.1016/j.compscitech.2007.07.005.

[22] M. Halvaei, M. Jamshidi, M. Latifi, M. Ejtemaei, Experimental investigation and modelling of flexural properties of carbon textile reinforced concrete, Constr. Build. Mater. 262 (2020), 120877, https://doi.org/10.1016/j.conbuildmat.2020.120877.

[23] D.H. Murcia, B. Çomak, E. Soliman, M.M. Reda Taha, Flexural Behavior of a Novel Textile-Reinforced Polymer Concrete, Polymers (Basel) 14 (2022) 1, https://doi.org/10.3390/polym14010176.

[24] Y. Du, X. Zhang, F. Zhou, D. Zhu, M. Zhang, W. Pan, Flexural behavior of basalt textile reinforced concrete, Constr. Build. Mater. 183 (2018) 7–21, https://doi.org/10.1016/j.conbuildmat.2018.06.165.

[25] K. Zdanowicz, S. Marx, Flexural behaviour of thin textile reinforced concrete slabs enhanced by chemical prestressing, Eng. Struct. 256 (2022) 113946, https://doi.org/10.1016/j.engstruct.2022.113946.

[26] N. Williams Portal, L. Nyholm Thrane, K. Lundgren, Flexural behaviour of textile reinforced concrete composites: experimental and numerical evaluation, Mater. Struct. 50, 1 (2016) 4, https://doi.org/10.1617/s11527-016-0882-9.

[27] T. Tysmans, M. Wozniak, O. Remy, J. Vantomme, Finite element modelling of the biaxial behaviour of high-performance fibre-reinforced cement composites (HPFRCC) using concrete damaged plasticity, Finite Elem. Anal. Des. 100 (2015) 47–53, https://doi.org/10.1016/j.finel.2015.02.004.

[28] R. Chudoba, E. Sharei, A. Scholzen, A strain-hardening microplane damage model for thin-walled textile-reinforced concrete shells, calibration procedure, and experimental validation, Compos. Struct. 152 (2016) 913–928, https://doi.org/10.1016/j.compstruct.2016.06.030.

[29] E. Sharei, A. Scholzen, J. Hegger, R. Chudoba, Structural behavior of a lightweight, textile-reinforced concrete barrel vault shell, Compos. Struct. 171 (2017) 505–514, https://doi.org/10.1016/j.compstruct.2017.03.069.

[30] A. Van Driessche, D.G. Aggelis, E. Tsangouri, Complex fracture on thin-wall textile reinforced cement (TRC) shells monitored by acoustic emission, Thin-Walled Struct. 167 (2021), 108216, https://doi.org/10.1016/j.tws.2021.108216.

[31] P. Rawat, et al., A state-of-the-art review on mechanical performance characterization and modelling of high-performance textile reinforced concretes, Constr. Build. Mater. 347 (2022), 128521, https://doi.org/10.1016/j.conbuildmat.2022.128521.

[32] R. Fangueiro, Fibrous and Composite Materials for Civil Engineering Applications, 1st ed., Woodhead Publishing, 2011.

[33] W.E. Weber, V. Mechtcherine, Modeling the dynamic properties of fibre-reinforced concrete with different coating technologies of multifilament yarns, Cem. Concr. Compos. 73 (2016) 257–266, https://doi.org/10.1016/j.cemconcomp.2016.07.017.

[34] J. Hegger, N. Will, O. Bruckermann, S. Voss, Load–bearing behaviour and simulation of textile reinforced concrete, Mater. Struct. 39 (8) (2006) 765–776, https://doi.org/10.1617/s11527-005-9039-y.

[35] I.G. Colombo, A. Magri, G. Zani, M. Colombo, M. di Prisco, Erratum to: Textile Reinforced Concrete: experimental investigation on design parameters, Mater. Struct. 46 (11) (2013) 1953–1971, https://doi.org/10.1617/s11527-013-0023-7.

[36] W. Brameshuber, "State-of-the-Art report of RILEM Technical Committee TC 201-TRC 'Textile Reinforced Concrete,'" 2006.

[37] A. Peled, A. Bentur, Geometrical characteristics and efficiency of textile fabrics for reinforcing cement composites, Cem. Concr. Res. 30 (5) (2000) 781–790, https://doi.org/10.1016/S0008-8846(00)00239-8.

[38] A. Sciegaj, F. Larsson, K. Lundgren, Experiments and calibration of a bond-slip relation and efficiency factors for textile reinforcement in concrete, Cem. Concr. Compos. 134 (2022), 104756, https://doi.org/10.1016/j.cemconcomp.2022.104756.

[39] M.C. Rampini, G. Zani, M. Colombo, M. di Prisco, Mechanical behaviour of TRC composites: experimental and analytical approaches, Appl. Sci. 9 (2019) 7, https://doi.org/10.3390/app9071492.

[40] A. Si Larbi, A. Agbossou, P. Hamelin, Experimental and numerical investigations about textile-reinforced concrete and hybrid solutions for repairing and/or

strengthening reinforced concrete beams, Compos. Struct. 99 (2013) 152–162, https://doi.org/10.1016/j.compstruct.2012.12.005.

[41] U. Häußler-Combe, J. Hartig, Bond and failure mechanisms of textile reinforced concrete (TRC) under uniaxial tensile loading, Cem. Concr. Compos. 29 (4) (2007) 279–289, https://doi.org/10.1016/j.cemconcomp.2006.12.012.

[42] A. Romanazzi, D.V. Oliveira, R.A. Silva, An analytical bond stress-slip model for a TRM composite compatible with rammed earth, Constr. Build. Mater. 310 (2021), 125228, https://doi.org/10.1016/j.conbuildmat.2021.125228.

[43] H.Y. Zhang, H.Y. Liu, V. Kodur, M.Y. Li, Y. Zhou, Flexural behavior of concrete slabs strengthened with textile reinforced geopolymer mortar, Compos. Struct. 284 (2022), 115220, https://doi.org/10.1016/j.compstruct.2022.115220.

[44] I. Blomqvist, Textile Reinforced Concrete Structures - Bending tests of one-way slabs, Chalmers University of Technology, Gothenburg, 2021.

[45] A. Delibasic, R. Hayatleh, Tunna textilarmerade betongplattor: Provmetod för belastning i planet, Chalmers University of Technology, Gothenburg, 2019.

[46] "StoCrete R 40," 2023. https://www.sto.se/s/p/a1F2p00000NwOcUEAV/stocrete-r-40 (accessed Jan. 31, 2023).

[47] "SS-EN 12390-3:2019. Testing hardened concrete - Part 3: Compressive strength of test specimens." 2019.

[48] GOM Gmbh, "Aramis adjustable," 2022. https://www.gom.com/en/products/3d-testing/aramis-adjustable (accessed Feb. 10, 2022).

[49] GOM GmbH, "GOM Correlate," 2022. https://www.gom.com/en/products/gom-suite/gom-correlate-pro (accessed Feb. 10, 2022).

[50] DIANA FEA, "DIANA Finite Element Analysis, User's Manual, release 10.5." TNO Building and Construction Research, Delft, 2021.

[51] fib, "CEB-FIP Model Code 2010." Wiley-VCH Verlag GmbH & Co, Lausanne, Switzerland, 2010.

[52] E. Thorenfeldt, Mechanical properties of high-strength concrete and applications in design, 1987.

[53] D.A. Hordijk, Local Approach to Fatigue of Concrete, Delft University of Technology, Delft, 1991.